Journal of
Materials Chemistry A

PAPER

View Article Online
View Journal

Check for updates

Cite this: DOI: 10.1039/d1ta06828h

Control over interpenetration for boosting methane storage capacity in metal–organic frameworks†

Jing Tan,‡[a] Yu Tao,‡[a] Xiangyu Zhang,‡[a] Qing Wang,[a] Tengwu Zeng,[a] Zhaolin Shi,[a] Kyle E. Cordova,[b] Yongjin Lee,*[ac] Haiming Liu*[a] and Yue-Biao Zhang*[a]

Received 10th August 2021
Accepted 3rd September 2021

DOI: 10.1039/d1ta06828h

rsc.li/materials-a

Metal–organic frameworks (MOFs) have been recognized as prominent methane adsorbents for use in cleaner modes of transportation. Currently, ultrahigh methane deliverable capacity is required for use in heavy-duty vehicles and long-haul transportation under industrially and economically feasible working conditions. Herein, we show that control over interpenetration in MOFs can serve as a realistic strategy for boosting methane deliverable capacity without altering the underlying topology. Specifically, a new MOF, termed ST-150 (ST = ShanghaiTech University), is demonstrated to possess an high volumetric deliverable capacity of 244 $\mathrm{cm_{STP}}^3\ \mathrm{cm}^{-3}$, which stands at a ~70% improvement over its interpenetrated counterpart–MOF-150. Due to the control over interpenetration, ST-150's deliverable capacity surpasses that of an empty compressed natural gas tank by 20% at 298 K and 5.8–200 bar. Variable-temperature solid-state nuclear magnetic resonance (NMR) spectroscopy combined with molecular simulation of methane uptake reveals new insights into the importance of molecular dynamics and its impact on the accessible pore volume, and ultimately, deliverable capacity for on-board methane storage in MOF materials.

Introduction

Natural gas is an alternative fuel to diesel and petrol in green transportation.[1] Compared with compressed natural gas (CNG) and liquefied natural gas (LNG), adsorbed natural gas (ANG) is better positioned for on-board methane storage due to an increase in volumetric energy density that is provided by the use of porous materials.[2] Featuring designable frameworks, well-defined adsorptive sites, and superior porosity, metal–organic frameworks (MOFs) have been widely studied for on-board methane storage and subsequent use in ANG processes.[3] Several prominent MOFs have demonstrated high uptakes[4] and deliverable capacities[5–7] at pressures up to 35, 65, 80, or 100 bar. Recently, we and others have propelled these MOFs into methane storage applications with new, attractive working conditions that promote their use in heavy-duty vehicles and long-haul transportation.[8] Herein, we report a strategy for optimizing deliverable capacity at 298 K and 5.8–200 bar by controlling framework interpenetration in MOF materials.

Owing to the backpressure of an internal combustion engine, methane uptake below a minimal desorption pressure (P_{des}; *e.g.*, 5.8 bar)[1c] of a gas cylinder is considered to be unusable. Thus, the deliverable capacity is evaluated by subtracting the unusable uptake from the total uptake at a certain maximal working pressure (P_{ads}; Scheme 1). Several flexible MOFs[6] have shown optimal deliverable capacity based on a gate-opening mechanism (Scheme 1a, red). In such systems, a MOF switches from a contracted state, thereby minimizing the unusable uptake, to an expanded state that maximizes the total uptake under working pressures (P_{ads}). However, in most of these systems, control over the flexibility in MOFs is not straightforward because there is potential for the MOF to become trapped in a gate-closed state under prescribed pressures (Scheme 1a, blue).

Interpenetration[9] has merit as a controllable alternative method to use when tuning MOF adsorption properties,[10] albeit the impact of interpenetration on ultrahigh-capacity methane storage has yet been reported. Herein, we illustrate how control over interpenetration in MOFs can be utilized to boost the deliverable capacity of a doubly interpenetrated MOF that imposes higher unusable methane uptake (Scheme 1b, blue)[10] to a non-interpenetrated MOF displaying higher total methane

---

[a] School of Physical Science and Technology, ShanghaiTech University, Shanghai 201210, China. E-mail: zhangyb@shanghaitech.edu.cn; leeyj@shanghaitech.edu.cn; liuhm@shanghaitech.edu.cn

[b] Materials Discovery Research Unit, Advanced Research Centre, Royal Scientific Society (RSS), 11941 Amman, Jordan

[c] Department of Chemical Engineering, Inha University, Incheon 22212, Republic of Korea

† Electronic supplementary information (ESI) available: Experimental details, and additional figures and tables. CCDC 2102603 and 2102604. For ESI and crystallographic data in CIF or other electronic format see DOI: 10.1039/d1ta06828h

‡ These authors contributed equally.

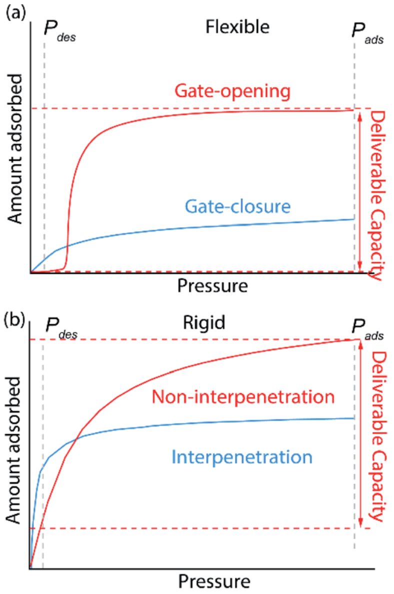

Scheme 1 Strategies for optimizing the deliverable capacity of on-board methane storage in MOFs. (a) Adsorption isotherms of a flexible MOF that experiences a gate-opening phenomena (red) in order to achieve optimal deliverable capacity. As a result of gate-closure (blue), the MOF fails to achieve an optimal deliverable capacity under the prescribed working pressure. (b) Adsorption isotherms of rigid MOFs with controlled interpenetration (red). The rigidity of the framework minimizes the unusable uptake while, at the same time, improving the total uptake in order to achieve optimal deliverable capacity. When the framework is interpenetrated (blue), the MOF exhibits compromised deliverable capacity.

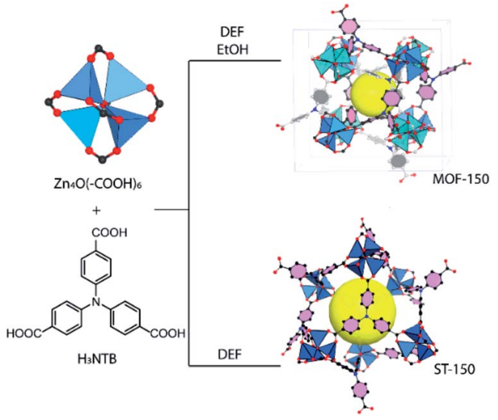

Fig. 1 Solvent-directing strategy for constructing the crystal structures of MOF-150 and ST-150. The solvents used for producing single crystals: MOF-150, DEF and EtOH; ST-150: DEF. Colour codes: Zn, light blue; C, black; O, red; N, blue. One of the interpenetrated frameworks in MOF-150 was dimmed for clarity.

uptake (Scheme 1b, red). Indeed, this strategy yields an optimal MOF system that is marked by its ultrahigh capacity for use in on-board methane storage processes.

Results & discussion

Syntheses and characterization

As a proof-of-concept, the iconic MOF-150 (Fig. 1), $[Zn_4O(NTB)_2]$,[11] that adopts the doubly interpenetrated pyrite net (**pyr-C2**) was pursued for this study. This MOF is constructed from $Zn_4O(-COO)_6$ and 4,4′,4″-nitrilotribenzoate (NTB) building units in DEF/EtOH (DEF = *N*,*N*-diethylformamide; EtOH = ethanol). A second counterpart MOF, ST-150 (Fig. 1, ST = ShanghaiTech University), adopting the non-interpenetrating **pyr** net, was realized using the same conditions with the notable exception of the solvent system, which in this case anhydrous DEF alone was employed (Section S1 in ESI†). The successful control over interpenetration in ST-150 is realized by reducing the amount of aprotic solvent used in the solvothermal synthesis. When the volumetric ratios of DEF to EtOH were varied from 7 : 3 to 9 : 1, several new X-ray diffraction peaks (Fig. 2a, *e.g.*, $2\theta = 6.8$, 8.8, and 13.0°) were observed suggesting the formation of non-interpenetrated ST-150 (Fig. 2b). This phenomenon is also consistently observed when switching solvent systems from DEF/EtOH to DEF/methanol and DEF/H_2O (Fig. S1†). We speculate that the formation of interpenetration in this system is sensitive to water content in DEF, which might facilitate the formation of framework interpenetration-directing $Zn(OH)_2$ units within the pores.[12]

While the crystal structure of MOF-150 was obtained relatively easily, the resolution of single-crystal X-ray diffraction for ST-150 was too poor to allow for structure elucidation. Accordingly, the crystal structure of ST-150 was characterized by synchrotron powder X-ray diffraction (PXRD, Section S2 in ESI†) using Rietveld refinement (Fig. 2c) against a non-interpenetrated model (Fig. S8, Tables S1–S2†). This analysis method resulted in satisfactory convergence ($R_{wp} = 7.92\%$ and $R_p = 5.79\%$). ST-150 crystalized in the chiral cubic $P2_13$ (no. 198) space group with a lattice constant of 22.440(5) Å. The framework adopts the non-interpenetrated **pyr** net and the void fraction reaches up to 76.2% of crystal volume (8616.6 Å^3 of the 11 299.6 Å^3 unit cell volume). The porous structure features interconnected cages with an internal pore diameter of 11.5 Å. For comparison, MOF-150 (Fig. S9, Tables S3–S4†) crystalizes in the centrosymmetric cubic $Ia\bar{3}$ (no. 206) space group with a lattice constant of 22.329(3) Å. The void fraction of MOF-150 is 39.8% and the structure is highlighted by its continuous channels with an internal pore diameter of 7.35 Å.

To compare their respective porosities, ST-150 and MOF-150 were fully activated (Fig. S2–S6†) by applying vacuum and heating at 120 °C for 24 h. N_2 adsorption isotherms at 77 K for both exhibit typical Type-I sorption behaviours (Fig. 2d and S10†) that are characteristic of microporous materials. The N_2 gas uptakes at $P/P_0 = \sim 1.0$ are 500 and 320 cm_{STP}^3 cm^{-3}, respectively, and their pore volumes are calculated to be 1.23 and 0.44 cm^3 g^{-1}, respectively. The multipoint BET plot of the N_2 adsorption isotherms (Fig. S11–S14†) affords specific surface areas of 3008 and 1082 m^2 g^{-1} for ST-150 and MOF-150, respectively. Narrow pore size distributions centred at 10.9 and 7.5 Å (Fig. 2d, inset), for ST-150 and MOF-150, respectively, were determined by fitting the Ar adsorption isotherms at 87 K

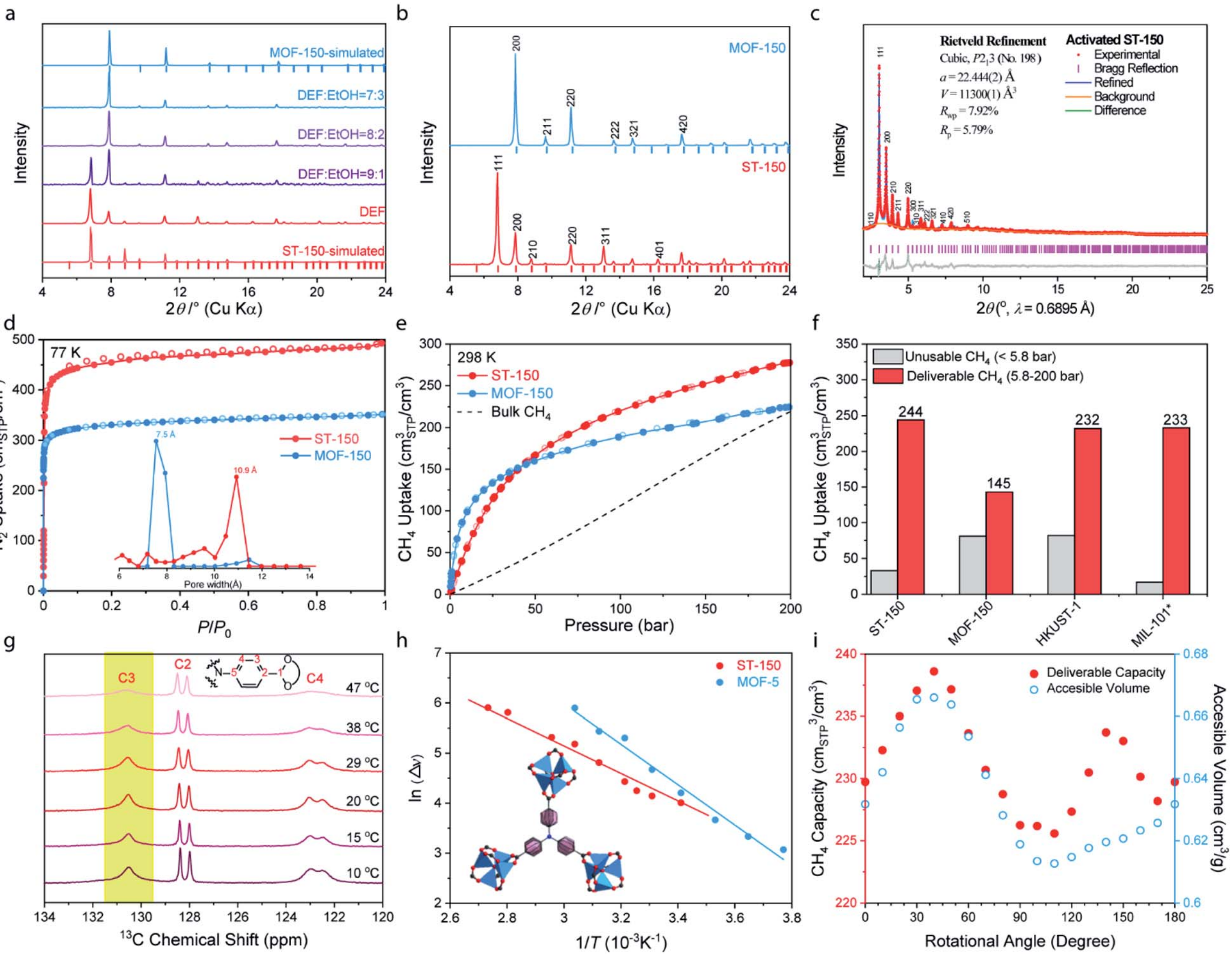

Fig. 2 (a) Control experiment of the solvent directing strategy for interpenetration control as analysed by PXRD patterns; (b) comparison of PXRD patterns of ST-150 and MOF-150; (c) synchrotron PXRD patterns of activated ST-150 and the Rietveld refinement against a non-interpenetrated model; (d) N_2 adsorption isotherms at 77 K for ST-150 and MOF-150 and the pore size distribution derived from their Ar adsorption isotherms at 87 K (inset); (e) high-pressure (0–200 bar) methane uptake at 298 K for ST-150 and MOF-150; (f) comparison of unusable methane and deliverable capacity (5.8–200 bar) of ST-150 to those of MOF-150 and other benchmark MOFs. *MIL-101 methane uptake is at 303 K. (g) Variable-temperature solid-state ^{13}C NMR partial spectra of ST-150; (h) temperature dependence of the linewidth, $\Delta\nu$, in ST-150 and MOF-5. The solid line represents the least squares curve fitted with an exponential function; (i) dependence of deliverable capacity of methane storage (from GCMC simulation) and accessible volume (from Zeo^{++} analysis) of ST-150 to the rotational angles of benzene ring from 0 to 180°.

(Fig. S15†). Indeed, these results are consistent with the pore metrics determined from their crystal structures. The data obtained from these gas sorption measurements validate the successful control of interpenetration from two-fold to none, while at the same time, in terms of volumetric porosity, both MOFs have similar surface areas (1634 and 1315 $m^2\ cm^{-3}$ for ST-150 and MOF-150, respectively), which has been considered as a figure of merit for volumetric capacity in methane storage.[5g]

High-pressure methane uptake

In order to evaluate methane storage performance of the interpenetrated (MOF-150) and non-interpenetrated (ST-150) MOF structures, methane adsorption isotherms at 298 K were measured from 0 to 200 bar (Fig. 2e, Section S4 in ESI†).

Total CH_4 adsorption is calculated using the equation:

$$n_{\text{tot}} = n_{\text{ex}} + V_{\text{p}} \times \rho_{\text{bulk}(p,T)};$$

where n_{tot} is the total adsorption, n_{ex} is excess adsorption, V_{p} is pore volume calculated from the N_2 uptake plateau, and $\rho_{\text{bulk(p,T)}}$ is the bulk gas density at different pressures and temperatures as obtained from the relevant U.S. National Institute of Standards and Technology database. Total CH_4 adsorption isotherms for each MOF were then fitted using Tóth Model[13] equations where n is the total amount adsorbed in mmol g^{-1}, P is the pressure in Pa, n_{L} is the saturation capacity in mmol g^{-1}, b is the parameter in Pa^{-1}, and t is the heterogeneity parameter of adsorbents.[13]

The total uptake of ST-150 is 278 $cm_{STP}^{3}\ cm^{-3}$ at 200 bar and 298 K (Fig. 2e) with the deliverable capacity being 243 $cm_{STP}^{3}\ cm^{-3}$ over the pressure range of 5.8 to 200 bar. Interestingly, this capacity is ~70% higher than that of MOF-150 (145 $cm_{STP}^{3}\ cm^{-3}$) and rivals the deliverable capacities achieved by the benchmark MOF materials (Fig. 2f), HKUST-1 (232 $cm_{ST}^{3}\ cm^{-3}$) and MIL-101 (233 $cm_{STP}^{3}\ cm^{-3}$ at 300 K). By fitting the methane isotherms at three distinct temperatures (273, 283, and 298 K, Fig. S19–S20†) with a virial equation (Fig. S21–S22†), the zero-coverage heat of adsorption (Fig. S23†) of ST-150 was calculated as 12 kJ mol^{-1}, which is much lower than that of the MOF-150 (19 kJ mol^{-1}). This result indicates that control over interpenetration reduces unusable uptake from 78 to 34 cm$_{\text{STP}}$^{3} cm^{-3} at 5.8 bar with relatively lower heat of adsorption.

Solid-state NMR spectroscopy

The high uptake and deliverable capacity of ST-150 benefit from inherent linker motion, framework flexibility, and crystal lattice dynamics, all of which have been considered as positive attributes of MOFs for high-capacity methane storage.[7] To verify the high porosity, high crystallinity, and linker dynamics of MOFs, in-depth solid-state NMR spectroscopic studies were carried out on the activated MOF-5, ST-150, and MOF-150.

Variable-temperature (VT) ^{1}H solid-state NMR spectroscopy were performed at 248–393 K (Section S5 in ESI†). ^{1}H spin-lattice relaxation time T_1 was measured using inversion-recovery sequence under nitrogen (Fig. S24 and Table S5†), showing typical T_1 for MOF-150 (2–3 s), much longer T_1 for ST-150 (14–17 s), and surprisingly, exceptionally longer T_1 for MOF-5 (115–119 s), which indicates a remarkable trend of increasing framework flexibility that is in consistence with higher porosity.[14] Furthermore, we revealed that when measuring under dry air the T_1 become significantly shorter (Fig. S24 and Table S6†) to various extents for MOF-5 (0.6–1.0 s), ST-150 (0.3–0.5 s) and MOF-150 (0.15–0.3 s). Such T_1 reduction is attributed to the strong paramagnetic relaxation effect of O_2 in the air, which is similar to the case of observed ^{29}Si T_1 reduction in zeolites.[15] Therefore, under air we can greatly enhance NMR sensitivity and dramatically speed up the spectral acquision by 10–100 times, which provides a new efficient methodology to access high-resolution a ^{1}H–^{13}C cross-polarization magic angle spinning (CPMAS) NMR spectroscopy of MOFs.

O_2-enhanced ^{13}C CPMAS solid-state NMR spectroscopy is implemented on activated MOF-5, ST-150, and MOF-150 to characterize molecular dynamics with slower motion for the first time in MOFs *via* linewidth analysis based on a transverse relaxation approach.[16] The VT ^{13}C CPMAS NMR spectra of MOF-5, ST-150 and MOF-150 are well resolved with all chemical shift assigned (Fig. S25–S27†). The assignments of tertiary and quaternary carbons in ST-150 and MOF-150 have been validated by varying the CP contact time (Fig. S27–S28†), which facilitated the study of phenyl ring dynamics based on the off-axis C–H.

For the organic linker (1,4-benzenedicarboxylate; BDC) in MOF-5 (Fig. S25†), the sharp C3 signal at 265 K (22 Hz in linewidth at 128.9 ppm) broadened significantly upon heating until reaching a maximum of $\sim$400 Hz above 363 K. In contrast, the linewidths of the C1 (COO) and C2 signals (both 7 Hz at 265 K) increased modestly to 20–40 Hz. This suggests that the phenyl ring re-orients around the two-fold C1–C1' axis (a so called π flip) at rates in the order of ^{1}H decoupling frequency.

Similarly, in the ^{13}C CPMAS NMR spectra of ST-150, the peaks of C3 and C4 are broadened along with increasing temperature reaching maxima (Fig. 2g), while C1, C2, and C5 signals increase to a lesser extent, which results from the same π flip of phenyl rings. More interestingly, at temperatures as low as 248 K (Fig. S26†), the two ring C–Hs, C3 and C4, each displayed four resolved peaks, corresponding to the four crystallographic independent sites in its crystal structure (Fig. S8†). With increasing temperature, the C3 signals gradually broaden and merge into one resonance centred at 129–132 ppm with a broad component underneath, and C4 signals become two resonances at 121–123 ppm, until reaching maximal linewidth at 373 K. Such dynamic spectral features are characteristic of a π flip of phenyl rings from two inequivalent linkers. In contrast, no temperature dependence of line broadening was observed in those of the MOF-150 (Fig. S27†).

Analysis of the C3 linewidth dependence on temperature over the range of 293 to 373 K, assuming an Arrhenius activation process,[16] yielded an activation energy (E_a) of 26.6 and 33.6 kJ mol^{-1} for ST-150 and MOF-5, respectively (Fig. 2h and Table S7†). These activation energies are close to that of MFM-115 (40 kJ mol^{-1}) that has a similar (–Ph)$_3$N motif.[7b] It is worth noting that the present methodology bypassed the difficulty in deuterium enrichment of organic linkers required for ^{2}H NMR, and yield precise dynamics information on the same natural abundant materials for gas storage. The observed lower activation energy of rotational dynamics might enable reorientation of benzene rings to optimize the methane packing at higher pressures, which has been recognized as a favourable feature for MOFs to achieve higher deliverable capacity.[7a]

Grand canonical Monte Carlo simulation

To investigate the impact of the dynamic motion on adsorption of methane in ST-150, we performed grand canonical Monte Carlo (GCMC, Section S6 in ESI†) simulations. The methane adsorption isotherm at 298 K was estimated by performing a GCMC simulation implemented in RASPA 2.0.[17] In GCMC simulations, the framework was regarded as rigid. Methane was described by the one site united-atom model with the parameters obtained from TraPPE force field. Because a methane molecule is neutral in the TraPPE forcefield, no electrostatic interaction was considered between CH_4 and the MOF. Dispersion interaction energies for MOFs were computed using a Lennard-Jones (LJ, Table S8†) potential form with parameters from the Dreiding force field. The Lorentz–Berthelot mixing rule was used for the pairwise interaction parameters. All pairwise interactions were truncated and shifted to zero at a distance of the cut-off radius of 12 Å. A simulation box was prepared by expanding a MOF unit cell repeatedly to ensure that the dimensions along each x, y, or z direction is at least twice the cut off radius. A total of 400 000 MC cycles with random translation, rotation, swap, and regrowth (*i.e.*, insertion) moves were used in each simulation; 2×10^5 cycles for equilibrium and the other 2×10^5 cycles for production.[17a] Considering the significant effect of linker orientation and phase transition on methane adsorption[7a], we rotated the linker of ST-150 from 0 (*i.e.*, the original ST-150) to 180° and the adsorption isotherm of methane was estimated at 298 K over the pressure range of 0–200 bar (Fig. S30†). The maximum methane uptake of ST-150 occurs when the benzene rings rotate with 40° – this leads to 20 $cm^3\ cm^{-3}$ higher uptake than that of the case when rotation happens with 100°. The trend in the variation of methane uptake upon linker rotation is found to be similar to that of the variation of accessible volume of ST-150 (Fig. 2i). The accessible volume exhibits 10% improvement from 0.61 to 0.67 $cm^3\ g^{-1}$, which allows the framework to adsorb more methane molecules at high pressure.[18]

Conclusions

In summary, by control over interpenetration, ST-150's deliverable capacity reaches as high as 244 $cm^3\ cm^{-3}$ for on-board methane storage at 298 K and 5.8–200 bar. This is a ~70% enhancement in comparison with its counterpart MOF-150 and surpasses those of the benchmark materials, HKUST-1 and MIL-101. The high deliverable capacity in ST-150 benefits from a lower heat of adsorption, which decreases the unusable methane uptake, as well as the molecular dynamics for enabling dynamic motions of benzene rings to have more accessible volume for higher methane uptakes. This result illustrates the feasibility of an alternate strategy of control over interpenetration for ultrahigh capacity methane storage by tailoring the porosity and molecular dynamics.

Author contributions

J. T. carried out the synthesis and characterization of MOFs. Y. T and Z. Shi conducted the high-pressure methane adsorption. X. Z. and Y. L. performed the molecular simulation. Q. W., T. Z. and H. L. conducted the solid-state NMR study. J. T., Y. T., K. E. C. and Y.-B. Zhang finalized the manuscript. The project was jointly led by H. L., Y. L. and Y.-B. Z.

Conflicts of interest

There are no conflicts to declare.

Acknowledgements

This work is supported by the Science and Technology Commission of Shanghai Municipality (21XD1402300), Start-up Fund from ShanghaiTech University, and the Alliance of International Science Organization (ANSO-CR-PP-2020-06). The authors acknowledge the support from Dr Min Peng and the Analytical Instrumentation Center (Contract no. SPST-AIC10112914) at ShanghaiTech University. The authors thank beamlines BL14B1 and BL17B at Shanghai Synchrotron Radiation Facility for providing beam time and assistance during experiments. We thank Prof. Hao-Long Zhou (Shantou University) for fruitful discussions.

Notes and references

1 (*a*) *BP Energy Outlook 2020 Edition*, https://www.bp.com; (*b*) *Shell LNG Outlook 2020*, https://www.shell.com; (*c*) Alternative Fuels Data Centre, Energy Efficiency & Renewable Energy, U.S. Department of Energy, https://www.afdc.energy.-gov/vehicles/natural_gas.html.

2 (*a*) *Methane Opportunities for Vehicular Energy, Advanced Research Project Agency-Energy*, U.S. Dept. of Energy, Funding Opportunity No. DE-FOA-0000672, 2012; (*b*) J. Wegrzyn and M. Gurevich, *Appl. Energy*, 1996, **55**, 71; (*c*) T. Burchell and M. Rogers, *SAE Tech. Pap. Ser.*, 2000-01-2205, 2000.

3 (*a*) S. Kitagawa, R. Kitaura and S. Noro, *Angew. Chem., Int. Ed.*, 2004, **43**, 2334; (*b*) T. A. Makal, J.-R. Li, W. Lu and H.-C. Zhou, *Chem. Soc. Rev.*, 2012, **41**, 7761; (*c*) A. Schoedel, Z. Ji and O. M. Yaghi, *Nat. Energy*, 2016, **1**, 16034; (*d*) Y. He, F. Chen, B. Li, G. Qian, W. Zhou and B. Chen, *Coord. Chem. Rev.*, 2018, **373**, 167.

4 (*a*) M. Eddaoudi, J. Kim, N. L. Rosi, D. T. Vodak, J. Wachter, M. O'Keeffe and O. M. Yaghi, *Science*, 2002, **295**, 469; (*b*) S. Ma, D. Sun, J. M. Simmons, C. D. Collier, D. Yuan and H.-C. Zhou, *J. Am. Chem. Soc.*, 2008, **130**, 1012; (*c*) Z. Guo, H. Wu, G. Srinivas, Y. Zhou, S. Xiang, Z. Chen, Y. Yang, W. Zhou, M. O'Keeffe and B. Chen, *Angew. Chem., Int. Ed.*, 2011, **50**, 3178; (*d*) H. Furukawa, N. Ko, Y. B. Go, N. Aratani, S. B. Choi, E. Choi, A. O. Yazaydin, R. Q. Snurr, M. O'Keeffe, J. Kim and O. M. Yaghi, *Science*, 2010, **329**, 424.

5 (*a*) Y. Peng, V. Krungleviciute, I. Eryazici, J. T. Hupp, O. K. Farha and T. Yildirim, *J. Am. Chem. Soc.*, 2013, **135**, 11887; (*b*) D. Alezi, Y. Belmabkhout, M. Suyetin, P. M. Bhatt, Ł. J. Weseliński, V. Solovyeva, K. Adil, I. Spanopoulos, P. N. Trikalitis, A.-H. Emwas and M. Eddaoudi, *J. Am. Chem. Soc.*, 2015, **137**, 13308; (*c*) J.-M. Lin, C.-T. He, Y. Liu, P.-Q. Liao, D.-D. Zhou, J.-P. Zhang and X.-M. Chen, *Angew. Chem., Int. Ed.*, 2016, **55**, 4674; (*d*) J. Jiang, H. Furukawa, Y. B. Zhang and O. M. Yaghi, *J. Am. Chem. Soc.*, 2016, **138**, 10244; (*e*) M. Zhang, W. Zhou, T. Pham, K. A. Forrest, W. Liu, Y. He, H. Wu, T. Yildirim, B. Chen, B. Space, Y. Pan, M. J. Zaworotko and J. Bai, *Angew. Chem., Int. Ed.*, 2017, **56**, 11426; (*f*) C.-X. Chen, Z.-W. Wei, J.-J. Jiang, S.-P. Zheng, H.-P. Wang, Q.-F. Qiu, C.-C. Cao, D. Fenske and C.-Y. Su, *J. Am. Chem. Soc.*, 2017, **139**, 6034; (*g*) Z. Chen, P. Li, R. Anderson, X. Wang, X. Zhang, L. Robison, L. R. Redfern, S. Moribe, T. Islamoglu, D. A. Gómez-Gualdrón, T. Yildirim, J. F. Stoddart and O. K. Farha, *Science*, 2020, **368**, 297; (*h*) C. Cuadrado-Collados, G. Mouchaham, L. Daemen, Y. Cheng, A. Ramirez-Cuesta, H. Aggarwal, A. R. Missyul, M. Eddaoudi, Y. Belmabkhout and J. Silvestre-Albero, *J. Am. Chem. Soc.*, 2020, **142**(31), 13391; (*i*) G. Verma, S. Kumar, H. Vardhan, J. Ren, Z. Niu, T. Pham, L. Wojtas, S. Butikofer, J. C. E. GarCia, Y.-S. Chen, B. Space and S. Ma, *Nano Res.*, 2021, **14**, 512; (*j*) B. Wang, X. Zhang, H. Huang, Z. Zhang, T. Yildirim, W. Zhou, S. Xiang and B. Chen, *Nano Res.*, 2021, **14**, 507.

6 (*a*) J. A. Mason, J. Oktawiec, M. K. Taylor, M. R. Hudson, J. Rodriguez, J. E. Bachman, M. I. Gonzalez, A. Cervellino, A. Guagliardi, C. M. Brown, P. L. Llewellyn, N. Masciocchi and J. R. Long, *Nature*, 2015, **527**, 357; (*b*) Q. Y. Yang, P. Lama, S. Sen, M. Lusi, K. J. Chen, W. Y. Gao, M. Shivanna, T. Pham, N. Hosono, S. Kusaka, J. J. t. Perry,

S. Ma, B. Space, L. J. Barbour, S. Kitagawa and M. J. Zaworotko, *Angew. Chem., Int. Ed.*, 2018, **57**, 5684; (*c*) T. Kundu, M. Wahiduzzaman, B. B. Shah, G. Maurin and D. Zhao, *Angew. Chem., Int. Ed.*, 2019, **58**, 8073.

7 (*a*) B. Li, H.-M. Wen, H. Wang, H. Wu, M. Tyagi, T. Yildirim, W. Zhou and B. Chen, *J. Am. Chem. Soc.*, 2014, **136**, 6207; (*b*) Y. Yan, D. I. Kolokolov, I. da Silva, A. G. Stepanov, A. J. Blake, A. Dailly, P. Manuel, C. C. Tang, S. Yang and M. Schröder, *J. Am. Chem. Soc.*, 2017, **139**, 13349; (*c*) F. Moreau, D. I. Kolokolov, A. G. Stepanov, T. L. Easun, A. Dailly, W. Lewis, A. J. Blake, H. Nowell, M. J. Lennox, E. Besley, S. Yang and M. Schröder, *Proc. Natl. Acad. Sci. U. S. A.*, 2017, **114**, 3056.

8 (*a*) A. U. Czaja, N. Trukhan and U. Müller, *Chem. Soc. Rev.*, 2009, **38**, 1284; (*b*) I. Senkovska and S. Kaskel, *Chem. Commun.*, 2014, **50**, 7089; (*c*) C.-C. Liang, Z.-L. Shi, C.-T. He, J. Tan, H.-D. Zhou, H.-L. Zhou, Y. Lee and Y.-B. Zhang, *J. Am. Chem. Soc.*, 2017, **139**, 13300; (*d*) Z.-L. Shi and Y.-B. Zhang, *Isr. J. Chem.*, 2018, **58**, 985.

9 H.-L. Jiang, T. A. Makal and H.-C. Zhou, *Coord. Chem. Rev.*, 2013, **257**, 2232.

10 (*a*) S. Ma, D. Sun, M. Ambrogio, J. A. Fillinger, S. Parkin and H.-C. Zhou, *J. Am. Chem. Soc.*, 2007, **129**, 1858; (*b*) H.-L. Jiang, Y. Tatsu, Z.-H. Lu and Q. Xu, *J. Am. Chem. Soc.*, 2010, **132**, 5586; (*c*) S. Bureekaew, H. Sato, R. Matsuda, Y. Kubota, R. Hirose, J. Kim, K. Kato, M. Takata and S. Kitagawa, *Angew. Chem., Int. Ed.*, 2010, **49**, 7660; (*d*) S. B. Choi, H. Furukawa, H. J. Nam, D. Y. Jung, Y. H. Jhon, A. Walton, D. Book, M. O'Keeffe, O. M. Yaghi and J. Kim, *Angew. Chem., Int. Ed.*, 2012, **51**, 8791; (*e*) J. Zhang, L. Wojtas, R. W. Larsen, M. Eddaoudi and M. J. Zaworotko, *J. Am. Chem. Soc.*, 2009, **131**, 17040; (*f*) O. K. Farha, C. D. Malliakas, M. G. Kanatzidis and J. T. Hupp, *J. Am. Chem. Soc.*, 2010, **132**, 950; (*g*) S. Yang, X. Lin, W. Lewis, M. Suyetin, E. Bichoutskaia, J. E. Parker, C. C. Tang, D. R. Allan, P. J. Rizkallah, P. Hubberstey, N. R. Champness, K. M. Thomas, A. J. Blake and M. Schroder, *Nat. Mater.*, 2012, **11**, 710; (*h*) A. Ferguson, J. Liu, S. J. Tapperwijn, D. Perl, F.-X. Coudert, S. V. Cleuvenbergen, T. Verbiest, M. A. van der Veen and S. G. Telfer, *Nat. Chem.*, 2016, **8**, 250.

11 (*a*) H. K. Chae, J. Kim, O. D. Friedrichs, M. O'Keeffe and O. M. Yaghi, *Angew. Chem., Int. Ed.*, 2003, **42**, 3907; (*b*) E. Y. Lee, S. Y. Jang and M. P. Suh, *J. Am. Chem. Soc.*, 2005, **127**, 6374.

12 (*a*) S. S. Kaye, A. Dailly, O. M. Yaghi and J. R. Long, *J. Am. Chem. Soc.*, 2007, **129**, 14176; (*b*) J. Hafizovic, M. Bjørgen, U. Olsbye, P. D. C. Dietzel, S. Bordiga, C. Prestipino, C. Lamberti and K. P. Lillerud, *J. Am. Chem. Soc.*, 2007, **129**, 3612; (*c*) H. Kim, S. Das, M. G. Kim, D. N. Dybtsev, Y. Kim and K. Kim, *Inorg. Chem.*, 2011, **50**, 3691.

13 (*a*) S. Cavenati, C. A. Grande and A. E. Rodrigues, *J. Chem. Eng. Data*, 2004, **49**, 1095; (*b*) J. Tóth, *Acta Chim. Acad. Sci. Hung.*, 1971, **69**, 311; (*c*) J. Tóth, *Adsorption: Theory, Modelling, and Analysis*, Marcel Dekker, New York, 2002.

14 (*a*) S. Horike, R. Matsuda, D. tanaka, S. Matsubara, M. Mizuno, K. Endo and S. Kitagawa, *Angew. Chem., Int. Ed.*, 2006, **45**, 7226; (*b*) S. Gould, D. J. Tranchmontagne, O. M. Yaghi and M. A. Garcia-Garibay, *J. Am. Chem. Soc.*, 2008, **130**, 3246; (*c*) C. S. Vogelsberg, F. J. Uribe-Romo, A. S. Lipton, S. Yang, K. N. Houk, S. Brown and M. A. Garcia-Garibay, *Proc. Natl. Acad. Sci. U. S. A.*, 2017, **114**, 13613; (*d*) J. T. Damron, J. Ma, R. Kurz, K. Saalwächter, A. J. Matzger and A. Ramamoorthy, *Angew. Chem., Int. Ed.*, 2018, **57**, 8678; (*e*) J. Perego, S. Bracco, M. Negroni, C. X. Bezuidenhout, G. Prando, P. Carretta, A. Comotti and P. Sozzani, *Nat. Chem.*, 2020, **12**, 845.

15 (*a*) D. J. Cookson and B. E. Smith, *J. Magn. Reson.*, 1985, **63**, 217; (*b*) J. Klinowski, T. A. Carpenter and J. M. J. Thomas, *Chem. Soc., Chem. Commun.*, 1986, 956; (*c*) H. Liu, H.-M. Kao and C. P. Grey, *J. Phys. Chem. B*, 1999, **103**, 4786; (*d*) H. Liu, H.-M. Kao and C. P. Grey, *The Proceedings of the Twelfth International Zeolite Conference*, Baltimore, 1998, p. 2317.

16 (*a*) W. P. Rothwell and J. S. Waugh, *J. Chem. Phys.*, 1981, **74**, 2721; (*b*) T. Ueda, K. Shimizu, H. Ohki and T. Okuda, *Z. Naturforsch.*, 1996, **51**, 910; (*c*) D. L. VanderHart, W. L. Earl and A. N. Garroway, *J. Magn. Reson.*, 1981, **44**, 361.

17 (*a*) D. Dubbeldam, S. Calero, D. E. Ellis and R. Q. Snurr, *Mol. Simulat.*, 2016, **42**, 81; (*b*) M. G. Martin and J. I. Siepmann, *J. Phys. Chem. B*, 1998, **102**, 2569; (*c*) S. L. Mayo, B. D. Olafson and W. A. Goddard, *J. Phys. Chem.*, 1990, **94**, 8897.

18 A. Luna-Triguero, J. M. Vicent-Luna and S. Calero, *Chem.–Eur. J.*, 2018, **24**, 8530.